Geologic Mapping Using Combined Analysis of Airborne Visible/Infrared Imaging Spectrometer (AVIRIS) and SIR-C/X-SAR Data

Fred A. Kruse

Analytical Imaging and Geophysics LLC, 4450 Arapahoe Ave., Suite 100, Boulder, Colorado 80303 USA
Phone: 303-499-9471, FAX: 303-665-6090, Email: kruse@aigllc.com

ABSTRACT

Hyperspectral imaging provides an efficient means of mapping surface mineralogy, however, mineralogic maps produced from these data do not take into consideration other geologic characteristics such as surface morphology and texture. Similarly, while advanced SAR systems such as the multifrequency, multipolarization SIR-C/X-SAR are well suited to mapping surface morphology parameters, they do not provide any mineralogic information. A combined approach provides significant advantages over individual use of either sensor. This research uses integrated analysis of Airborne Visible/Infrared Imaging Spectrometer (AVIRIS) and Shuttle Imaging Radar-C (SIR-C/X-SAR) data for geologic mapping. AVIRIS data were calibrated to reflectance, spectral endmembers were selected, and abundance images were generated for specific endmembers using spectral mixing and matched filtering. SIR-C images were synthesized from the complex scattering matrix data for selected frequency/polarization combinations and X-SAR data were coregistered to form a multifrequency, multipolarization data set. The SAR and AVIRIS data were map-referenced and analyzed together along with Landsat TM and Thermal Infrared Multispectral Scanner (TIMS) data using geometric visualization and analysis techniques developed for hyperspectral data analysis. The results provide an example of the viability of an extended spectral signature approach, segmenting the terrain into distinct lithologic units on the basis of combined mineralogic and morphologic characteristics. This approach has significant implications for future remote sensing missions and sensors. The research also demonstrates that multispectral and hyperspectral techniques can be successfully applied to combined optical/SAR data sets.

KEYWORDS: AVIRIS, TIMS, Thematic Mapper, SIR-C, X-SAR, Hyperspectral Imaging, Imaging Spectrometers, Radar, Data Integration, Mineral Mapping, n-Dimensional Visualization

1. Introduction

A combined digital image dataset consisting of Landsat Thematic Mapper (TM), Thermal Infrared Multispectral Scanner (TIMS), Airborne Visible/Infrared Imaging Spectrometer (AVIRIS), and Shuttle Imaging Radar-C (SIR-C/X-SAR) was used to map the composition and surface morphology in northern Death Valley, California, USA. These data were combined by co-registering TM bands and ratio images, TIMS bands and decorrelated images, mineral maps derived from AVIRIS data, and 3 each polarizations (HH, VV, HV) for both L-Band and C-Band SIR-C as well as X-VV polarization X-SAR data and SAR-derived surface roughness images. Color composite images were used as the starting point for analysis; the specific images and band combinations to use were selected based on known optical and SAR characteristics in specific wavelength regions. Several techniques developed for the analysis of imaging spectrometer (hyperspectral) data were then used for digital analysis of the combined data set[1, 2]. These include determination of the inherent dimensionality of the data and "spectral" dimension reduction based on the "Minimum Noise Fraction" (MNF) rotation, spatial dimension reduction using the "Pixel Purity Index" (PPI) to determine those pixels with unique characteristics in the combined data set, and interactive definition of "spectral" classes or training sets using n-Dimensional visualization techniques. Once these methods defined the "spectral" units present, image maps showing the relations between composition and morphology were generated using both classical and hyperspectral-based supervised classification techniques.

2. AVIRIS Data Analysis

2.1 AVIRIS Data

Airborne Visible/Infrared Imaging Spectrometer (AVIRIS) data used in this analysis were acquired on 21 July 1995. Four 614 pixel x 512 line x 224 band AVIRIS scenes covering an area at the north end of Death Valley (spatial coverage approximately 12 x 10 km per scene) were processed and analyzed. The AVIRIS data were calibrated to reflectance using the ATREM atmospheric model[3]. Preliminary interactive spatial and spectral browsing indicated the presence of clays, carbonates, iron oxides, zeolites, and minimal vegetation. Standardized procedures developed by AIG for AVIRIS processing were then applied to the 1995 AVIRIS data[4]. These included spectral reduction using a Minimum Noise Fraction (MNF) transformation[2, 5], spatial reduction using the "Pixel Purity Index (PPI)[1]and unconstrained linear spectral unmixing[6, 7].

2.2 Minimum Noise Fraction

A "Minimum Noise Fraction" (MNF) transformation[5] was used to determine the inherent dimensionality of the AVIRIS data (the number of individual endmembers in the scene). The MNF is a data transform similar to principal components (PC) transformations, which are commonly used to compress and/or enhance multispectral remote sensing data. Although PC transformations often result in components that show decreasing image quality with increasing component number, in some cases, particularly with aircraft data, some lower order components may contain significant information. The MNF transform is specifically designed as a linear transformation that maximizes the signal-to-noise ratio, thus ordering images in terms of decreasing image quality in lower order components[5]. Like PCs, the MNF transform can be used to determine the inherent dimensionality of image data, to segregate noise in the data, and to reduce the computational requirements for subsequent processing[1]. The MNF transformation requires that the noise covariance matrix of the data be known or estimated. Once the covariance is known, the first step of the transformation removes band-to-band correlations and rescales the noise in the data to have unit variance. The second step is a standard Principal Components transformation of the normalized data. Once transformed, increasing band numbers (lower order components) will have lower signal-to-noise ratios. The higher-order images will have large eigenvalues and spatially coherent eigenimages. The lower-order components will have low eigenvalues and the images will be noise-dominated. By using only the spatially coherent images in subsequent processing, the noise is separated from the data, thus improving processing results.

2.3 Pixel Purity Index (PPI)

Once the data dimensionality has been reduced in the spectral dimension using the MNF transformation, then the "Pixel-Purity-Index" (PPI)[8] was applied to the data to reduce the spatial dimensionality. The PPI is a means of finding the most "spectrally pure" (extreme) pixels in multispectral and hyperspectral images. The most spectrally pure pixels typically correspond to spectrally unique materials (often referred to as "endmembers"). The Pixel Purity Index is computed by repeatedly projecting n-dimensional scatterplots onto a random unit vector. The extreme pixels in each projection are recorded and the total number of times each pixel is marked as extreme is noted. PPI is in effect a means of reducing the spatial dimensions considered during subsequent training set selection. A PPI image is created in which the DN of each pixel corresponds to the number of times that pixel was recorded as extreme. The majority of pixels lie to the interior of the scatterplot and thus are never selected; thus the reduction of dimensionality. Thresholding of the PPI image to only the most extreme pixels results in further spatial reduction. Typically the ROI created during the thresholding procedure may consist of less than one percent of the original pixels.

2.4 N-Dimensional visualization and training set selection

The PPI image was used in this study to select training sets by using "N-Dimensional Visualization" to identify "spectral" endmembers. This approach to data analysis uses the distribution of the PPI-derived point spectra in n-space to estimate the number of endmembers and their pure signatures. An interactive tool for selecting the endmembers in n-space allows real-time "spinning" of the scatterplot. The inherent assumption of this method is that spectra can be thought of as points in an n-dimensional scatterplot, where n is the number of bands[1]. The coordinates of the points in n-space consist of "n" values that are simply DN values in each band for a given pixel. Interactive rotation of the scatterplots in 3-D and higher dimensions and projection of the points back to the 2-D space allows location and "painting" (alarming) of clusters of pixels with similar spectral characteristics. Continued rotation of the painted scatterplot discloses whether the points are clustered in N dimensions. If the points rotate together in 3-D or higher, then they form a unique "spectral" class. If they tend to separate, or the clusters break down in the higher dimension rotations, then further rotation is conducted until they consistently form discrete clusters and these clusters are painted again. Once all of the endmembers were marked, then they were exported to the image space and average spectra were extracted for use in further image analysis (Figure 1).

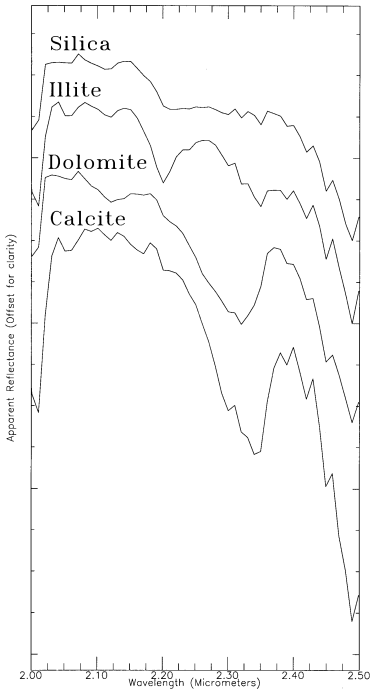

Figure 1. AVIRIS Unmixing Endmembers

2.5 Unconstrained Linear Spectral Unmixing

Endmember spectra extracted from the data using the techniques described above were used to conduct linear spectral unmixing to quantitatively map mineral abundances[1, 2, 4, 6, 7, 8]. The goal was to derive the apparent fractional abundance of each endmember material in each pixel, given a set of known spectral endmembers. In this case, a mixing endmember matrix made up of the image endmember spectra was inverted and multiplied by the observed spectra to get least-squares estimates of the unknown endmember abundance fractions[6]. Physical constraints indicate that the solution should give positive fractions that sum to unity, however, imposing these constraints on the data requires extensive computations. Personal experience (Kruse, unpublished data) indicates that the constrained model can take as much as 50 times longer to execute. Therefore, an iterative approach was taken for this analysis to achieve similar results. Unconstrained linear unmixing was performed with the endmembers derived using the PPI analysis. The resulting abundance images were examined to determine if the constraints were met, and an RMS error image was used to spatially locate areas with high errors. Additional endmember spectra were extracted from the high-RMS areas and the unmixing was performed again with the new endmember set. This procedure was repeated until all of the RMS errors were low, and the abundance images had positive fractions that summed to one. Once these criteria were met, then the physical constraints were satisfied. This procedure effectively results in a constrained unmixing result without actually having to run the constrained model and pay the computational penalty imposed by this model. Figure 2 shows a small spatial subset of the abundance images for the minerals calcite, dolomite, illite, and silica. Brighter pixels on the images represent higher abundances. Note the principal mineralogies at sites "A", "B", "C", "D", "E", "F", "G", "H", "I", and "J".

2.6 Georeferencing

Band 30 (0.66 μm) from each of the four scenes was used to construct a georeferenced mosaic. The four scenes were from two separate flightlines. Two scenes each from each flight line were joined together to form two mosaicked data sets. The two flightlines were histogram matched and georeferenced to UTM coordinates by using a previously map-registered SPOT image as the base image and picking approximately 240 ground control points (GCPs) for precision registration. Delaunay triangulation and nearest neighbor resampling were used to generate the single-band georeferenced mosaic. Mineral abundance images produced using the above analysis procedures were georeferenced using the same geometric model and GCPs. A small subset of this mosaic shown in Figure 1 corresponding to area of overlap of the AVIRIS, TM, TIMS, and SIR-C/X-SAR was used as the base area for further analysis.

3. SIR-C/X-SAR Data Reduction

The SIR-C data used for this study were acquired as DT120.30 on 16 April 1994 as part of the Space Radar Laboratory (SRL-1) shuttle mission STS-59[9]. The data were calibrated by the Jet Propulsion Laboratory (JPL) and HH, VV, HV, and total power images were synthesized from the compressed data products using algorithms provided by JPL. The X-SAR data were acquired at the same time as the SIR-C data. The X-SAR is a single-band X-VV polarization image. See additional references[9, 10, 11, 12, 13, 14] for additional information about SAR data, the SRL-1 and SRL-2 missions, and the SIR-C/X-SAR radar configurations and capabilities.

SAR data, rather than responding to compositional differences, interacts with surfaces to provide morphological information[11, 13]. Rough surfaces return large amounts of the transmitted energy to the SAR sensor, while smooth surfaces scatter the energy and thus have low radar returns. Other factors such as dielectric properties and radar characteristics (frequency, depression angle, polarization) can also affect the radar return. Figure 3 shows a small subset of the individual quad-polarization SIR-C images synthesized from the compressed scattering matrix as well as the standard X-SAR (X-VV) multilook detected image for the area of overlap with the other data sets. The dark areas on the images correspond to "smooth" surfaces, in this case, primarily older relict alluvial fans such as areas "B", "C", "F", "G", and "I". Brighter areas on the image such as area "A", "D", "E", and "H" represent high radar return, and thus rougher surfaces.

The L and C band SIR-C data were also used in a Small Perturbation Model (see Kierein-Young, 1996) to determine the parameters "RMS Surface Roughness" and "Fractal Dimension". These are direct geophysical measures of the surface roughness and roughness variability derived from inversion of the power spectra of the multifrequency data in a geophysical model. Unfortunately, in this case, the inversion results contain a high degree of variability and a low degree of spatial coherency. A 5 x 5 median filter was used to try to better show the spatial distribution of rough and smooth. Figure 3 also shows the RMS image. This image does discriminate light, rough areas from dark, smooth areas, however, because of the high

Figure 2. Northern Death Valley 1995 AVIRIS
Linear Spectral Unmixing Results

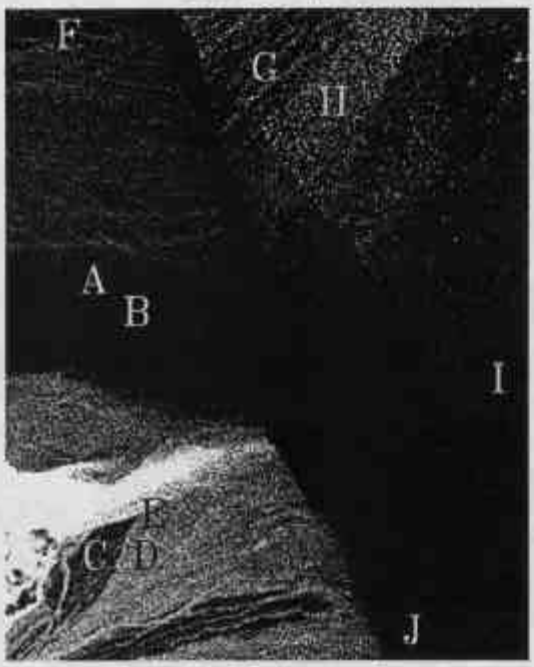

Calcite Endmember

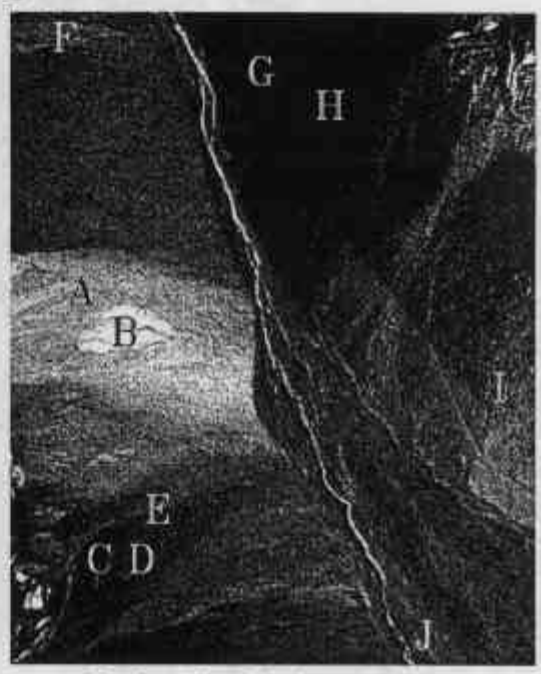

Dolomite Endmember

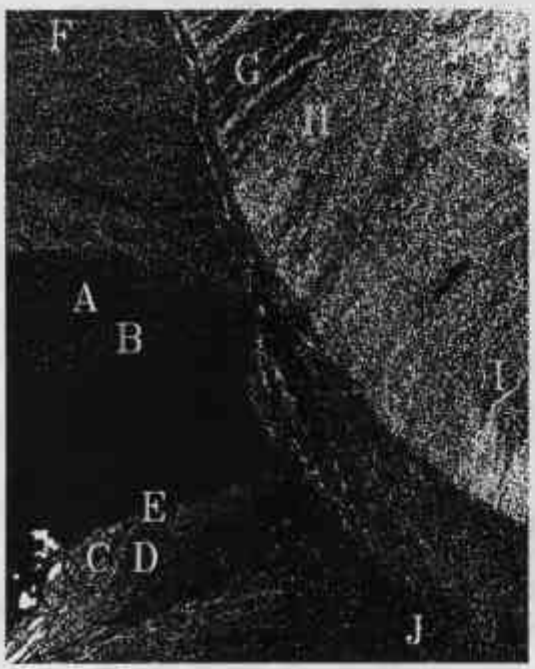

Illite/Muscovite Endmember

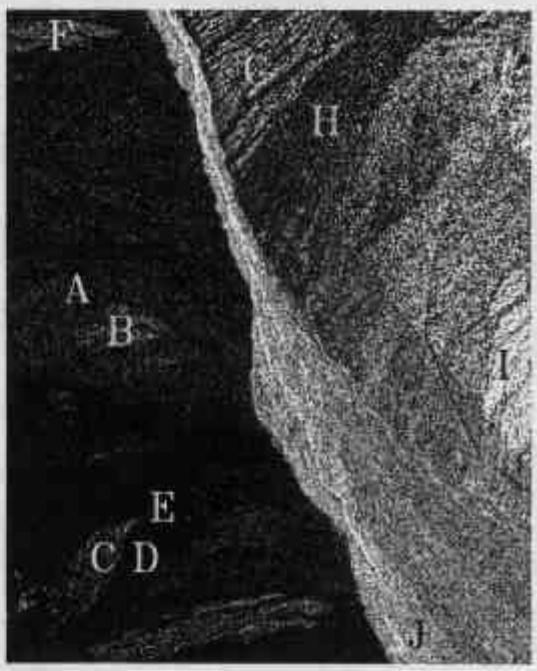

Silica Endmember

0 2 Kilometers

0 1 2 Miles

Figure 3. Northern Death Valley 1995 SAR Data
SIR-C/X-SAR Images

SIR-C L-VV

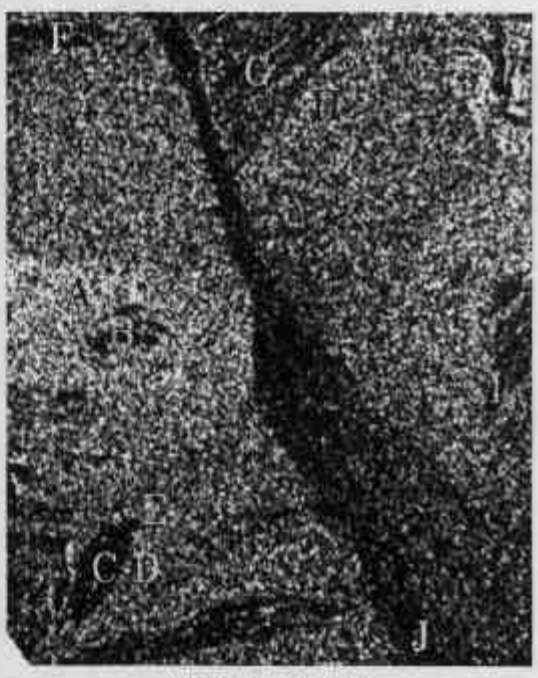

SIR-C C-VV

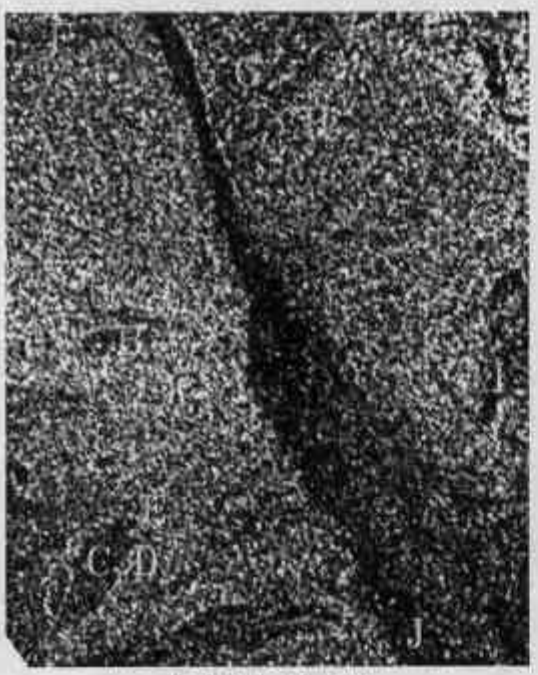

X-SAR X-VV

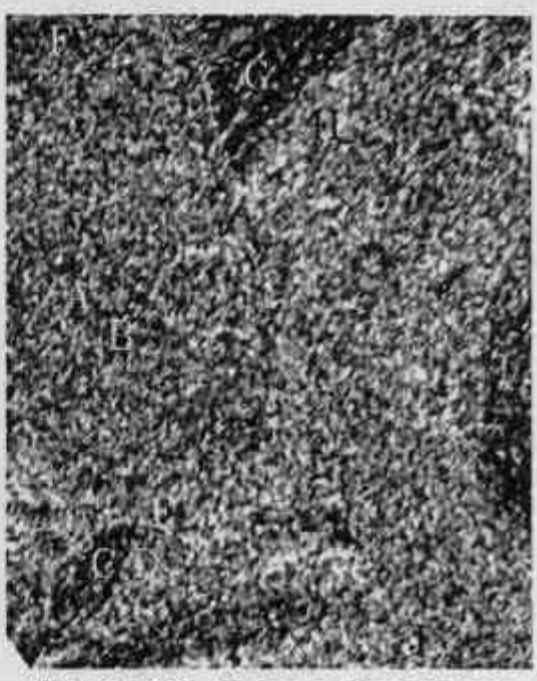

SIR-C RMS Surface Roughness

0 2 Kilometers

0 1 2 Miles

variability, it does not appear to produce significantly greater information than simply using the individual synthesized bands as a qualitative measure of rough versus smooth surfaces. The RMS image was not used in further digital analysis.

The X-SAR data were registered to the SIR-C data by picking control points and warping using Delaunay triangulation and nearest neighbor resampling. Both SAR data sets were then georeferenced to the map-referenced SPOT data using the same procedures.

4. Landsat TM and TIMS data

The Landsat Thematic Mapper (TM) data used in this analysis is a subscene of data acquired on October 8, 1984. Only the 6 visible and infrared bands were used. No preliminary processing was performed on the TM data. The Thermal Infrared Multispectral Scanner (TIMS) data are a 6-band multispectral data set covering the 8 - 12 micrometer range[15]. These data were acquired on 31 May 1992. The TIMS data were roughly corrected for temperature effects using a decorrelation stretch (d-Stretch)[16]. Comparisons of similar data sets to data calibrated to radiance and then to emissivity show that the d-stretch data approximate the emissivity data[17, 18, 19]. This is important, because in unprocessed (daytime) TIMS data, differential heating effects overwhelm the lithological signatures caused by emitted thermal infrared energy.

Color composites were formed from the TM dataset using common band combinations to optimize discrimination of specific materials. The TM data were viewed as both true-color (Bands 3, 2, 1 RGB) and color-infrared (Bands 4, 3, 2 RGB) composites. Other false color composites (eg: Bands 7, 5, 1 and band ratio images 5/7, 3/1, and 2/4 RGB) were also used to best discriminate areas containing clay/carbonates and iron oxides. Band ratios are typically used to enhance spectral differences between bands. Dividing one spectral band by a second band produces an image that can be used to determine relative band intensities. Combining three ratios into a color-ratio-composite (CRC) image allows determination of the approximate spectral shape for each pixel spectrum. Figure 4 shows grayscale images of two of the ratio images. These highlight clays/carbonates (areas "D", "E", and "H" on the 5/7 ratio), and iron oxides (areas "C" and "H" on the 3/1 ratio).

Raw TIMS data, when displayed as color composites typically contain few, low saturation colors. This is caused by the high correlation between bands attributed to the masking effect of differential heating (temperature)[17, 19]. The TIMS data were processed to approximate removal of the temperature effects using the decorrelation stretch (d-stretch) procedure as described by Gillespie and Kahle[16]. The "standard" decorrelated bands 5, 3, 1 (RGB) color composite was made to highlight areas of high silica. Figure 4 shows the TIMS d-stretch band 5 and 3 images (approximately 10.5 and 9.2 μm respectively). Bands 5 and 3 are complementary, as they are placed on the edge and center respectively of the silica restrahlen feature occurring near 9 μm. These images highlight areas having high concentrations of silica[17, 18, 19], which appear bright on the band 5 image and dark on the band 3 image. Specific examples of these high silica areas are "C", "D", "F", "G", "I", and "J", with the relative image brightness depending on the silica concentration (or in some cases the degree of mixing with other materials). The TM- and TIMS-derived images were georeferenced to the map-referenced SPOT data using Delaunay triangulation and nearest neighbor resampling.

5. Combined Analysis

5.1 Digital Analysis of Combined Dataset Using "Hyperspectral" Techniques

In order to bring some level of automation to the mapping process, it is necessary to use the combined data sets for digital analysis. This usually presents significant problems, however, because these data sets are of different data types (eg: byte data for the TM data versus floating point data for the SAR) and each data set has its own inherent data characteristics (eg: dynamic range, signal-to-noise ratio, etc.). For the purposes of combining these data sets, we have adapted the techniques described above[1, 2, 4, 7, 8] for the analysis of imaging spectrometer (hyperspectral) data for digital analysis of the combined data set. These include determination of the inherent dimensionality of the data and "spectral" dimension reduction based on the MNF rotation, spatial dimension reduction using the PPI to determine those pixels with unique characteristics in the combined data set, and interactive definition of "spectral" classes using the n-Dimensional visualization techniques. Similar approaches have been implemented with some success in the course of SIR-C research for this site[20, 21, 22, 23]. Once these methods have been used to define the "spectral" units present, generating a lithologic image map can be accomplished using any supervised classification technique. An example of the results from a spectral angle mapper (SAM) classification are described below.

The MNF transformation was performed on an 11-band combined data set consisting of the TM ratios (5/7 and 3/1), decorrelated TIMS bands (5 and 3), the AVIRIS mineral abundance images (calcite, dolomite, illite, silica), and selected

Figure 4. Northern Death Valley 1995 Optical Data
TM Ratios and TIMS Decorrelated Images

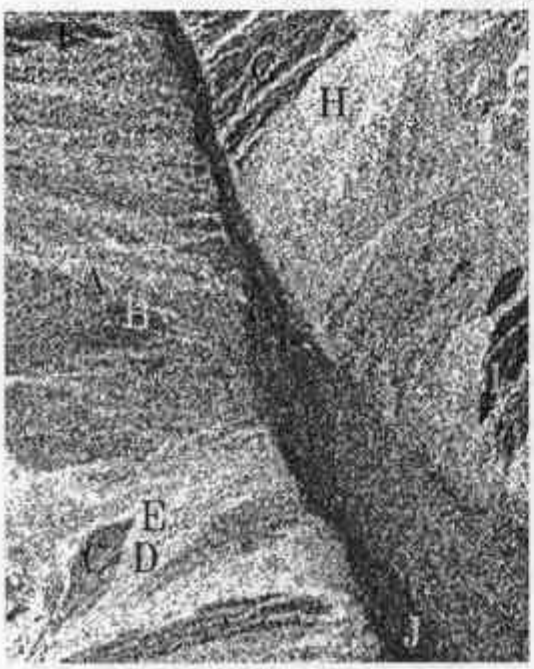

Landsat TM 5/7 Ratio

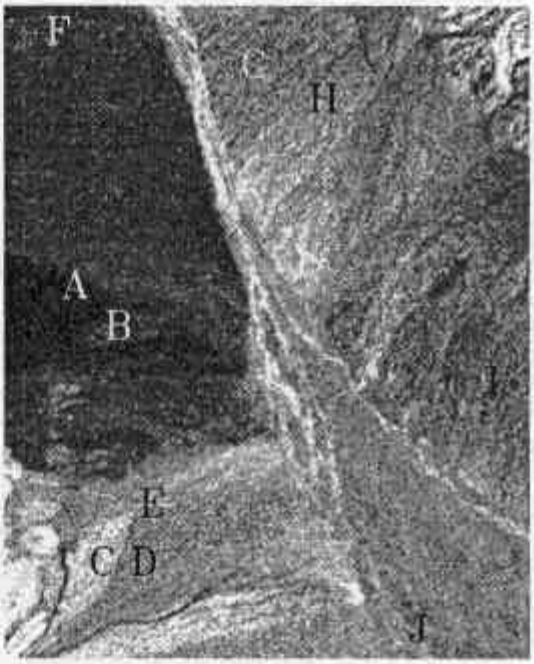

Landsat TM 3/1 Ratio

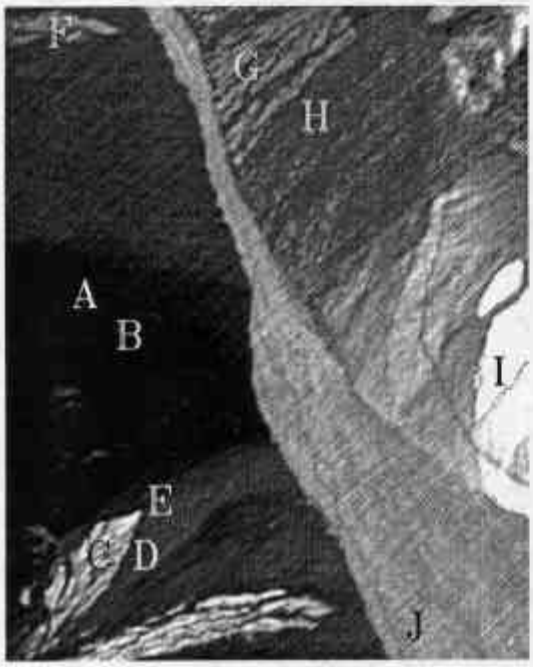

TIMS Decorrelated Band 5

0 2 Kilometers

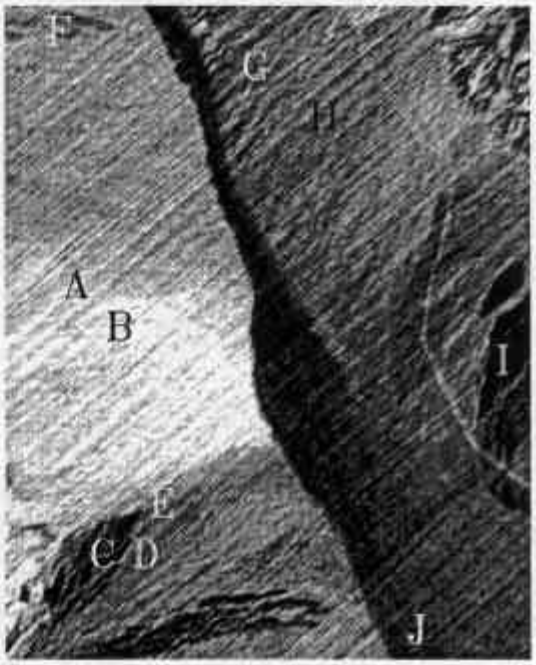

TIMS Decorrelated Band 3

0 1 2 Miles

Figure 5. Northern Death Valley 1995 Combined Optical/SAR Data
Selected MNF EigenImages

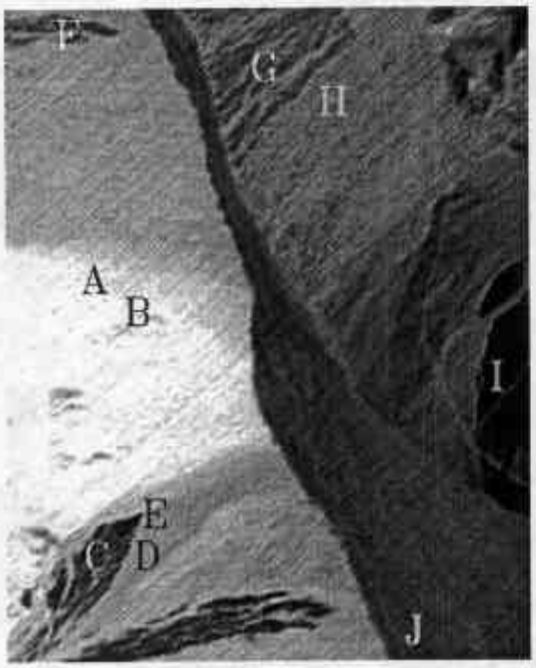

MNF Band 1

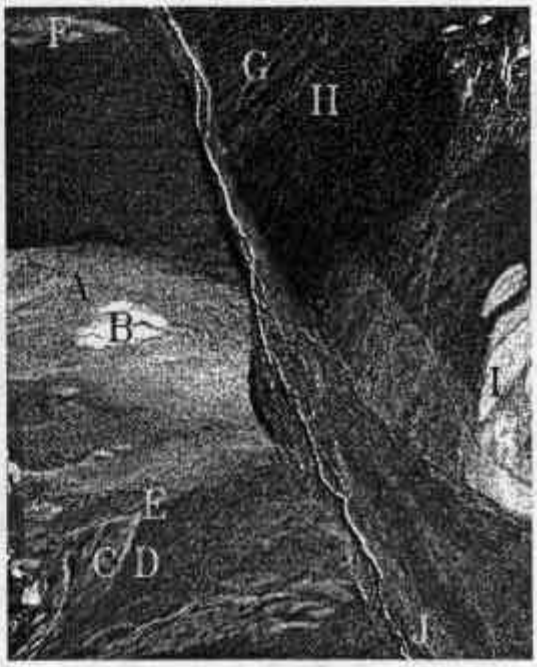

MNF Band 3

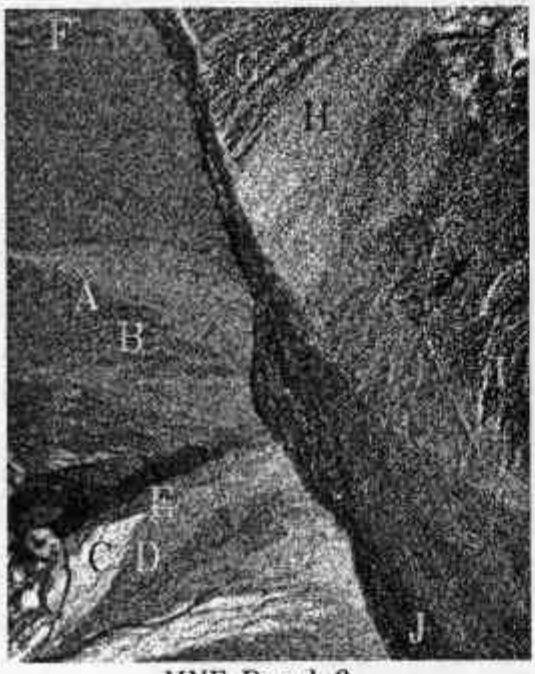

MNF Band 6

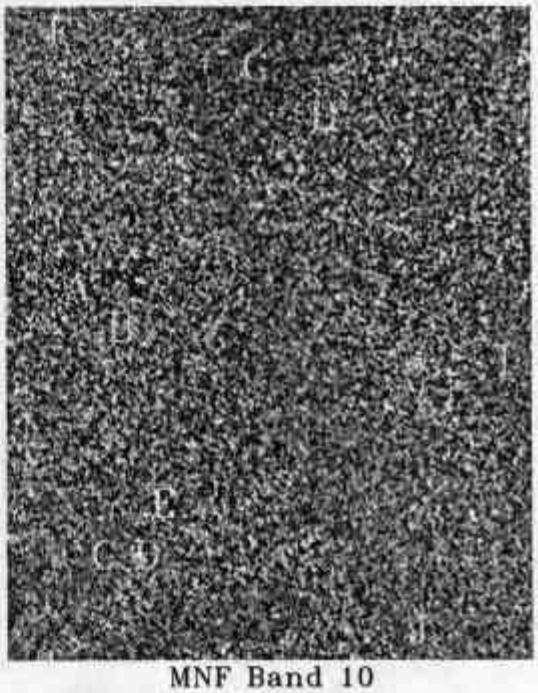

MNF Band 10

0 2 Kilometers

0 1 2 Miles

SIR-C/X-SAR bands (L-VV, C-VV, and X-VV). Figure 5 shows selected eigenimages for the MNF transform of the combined optical/SAR data set Green et al.[5] note, that unlike PCs, "because the MNF transform depends on signal-to-noise *ratios*, it is invariant under scale changes to any band". This is particularly important for the combined optical/SAR dataset used in this study, as each data type has its own data range and precision. Figure 6 shows a plot of the MNF eigenvalues. Clearly, most of the information is contained in the first few image bands.

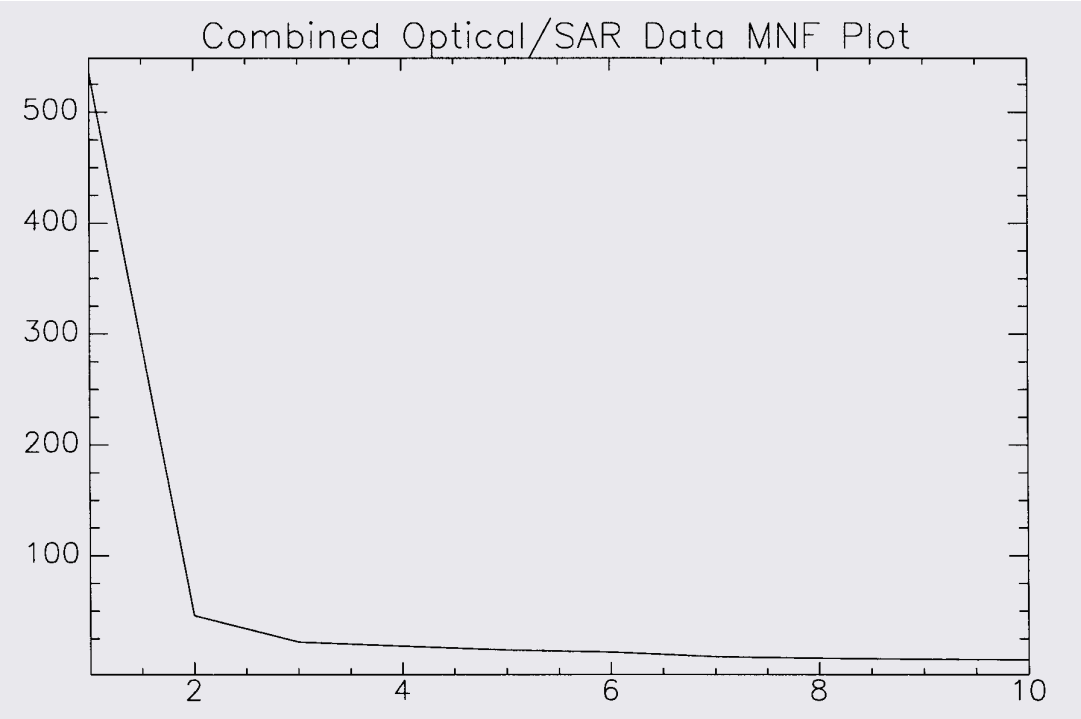

Figure 6. Eigenvalues (y-axis) for the MNF transformation of the combined data set. Horizontal axis is MNF Band

The PPI was run on the first 6 eigenimages (Figure 5) to determine the "spectrally" extreme pixels in the combined dataset. Note that the PPI only tells you which pixels have spectrally unique character, not which pixels group together into "units". A threshold was used to select around 2000 pixels from the PPI image for further analysis using "N-Dimensional Visualization" to identify "spectral" endmembers. This approach to hyperspectral data analysis is adapted here for use on the combined optical/SAR data set. As mentioned previously, the inherent assumption of this method is that spectra can be thought of as points in an n-dimensional scatterplot, where n is the number of bands. The concept is similar in this case, though we are not dealing with a "spectrum" per se because of the diverse and discontinuous nature of the combined data set.

The n-Dimensional Visualizer was used to spin the PPI-derived pixels in 6 dimensional space corresponding to the 6 eigenimages derived using the MNF procedure. The n-dimensional scatterplot was interactively rotated and coherent groups of pixels in the n-D plot were highlighted and exported to Regions of Interest (ROIs) as potential lithologic classes. These ROIs were then used to extract "spectra" from the combined data cube of derived images. Figure 7 shows selected combined "spectra" for the classes defined using the combined mineralogy/morphology determined from these images. Combining the plots for the different derived images. allows discrimination of the specific materials based on their full characteristics in the visible, near-infrared, short-wave infrared, thermal infrared, and microwave portions of the spectrum.

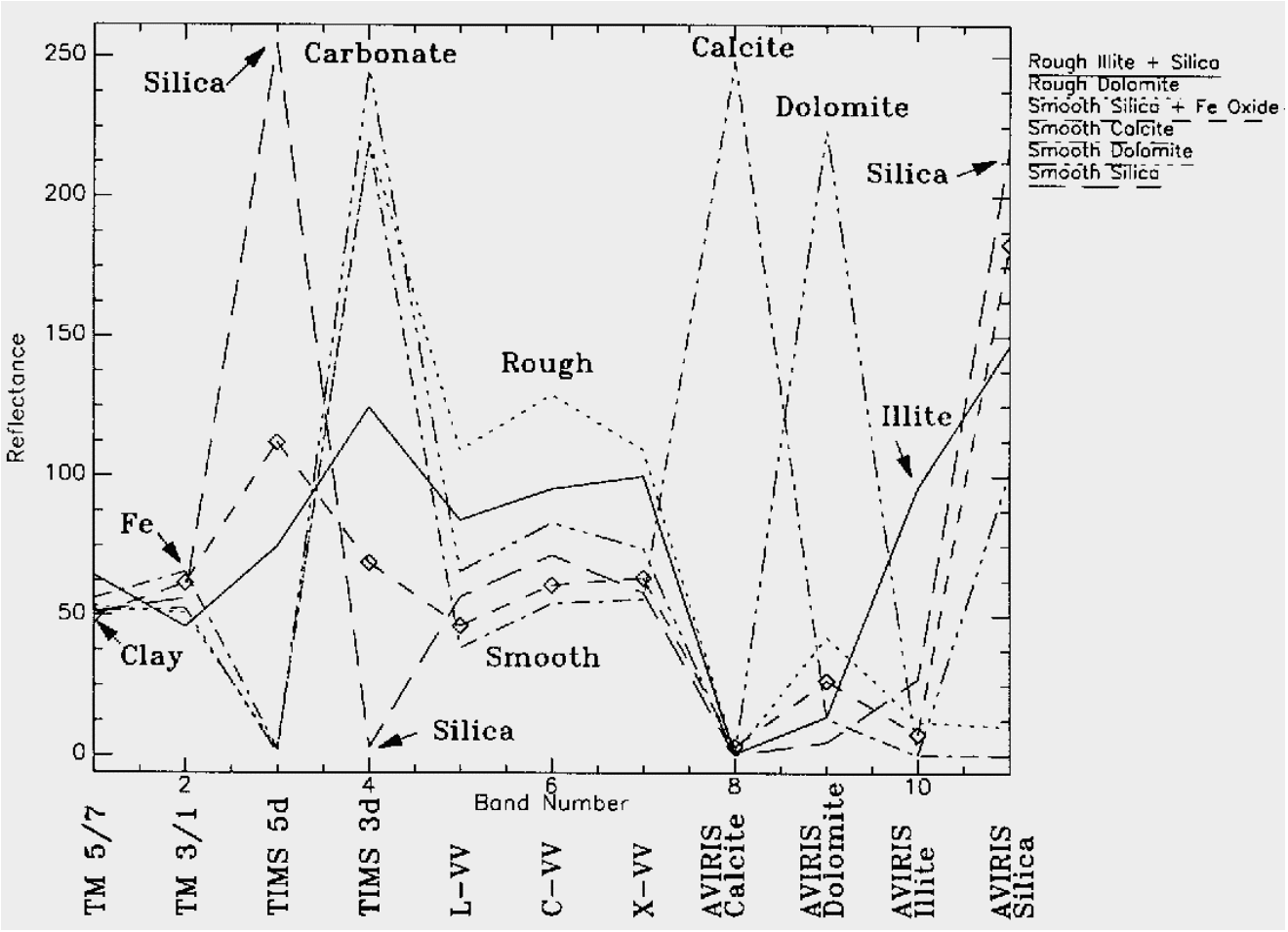

Figure 7. Extended "spectral" signatures for lithologic units extracted using the n-Dimensionsl Visualizer

Once the ROIs have been interactively defined and their characteristics examined based on interpretation of extracted mean plots as above, then they can be used in any supervised classification scheme. It should be noted that it is best to classify on the MNF data (using only the coherent bands) rather than the raw combined data sets. The resulting classified image represents an extremely detailed geologic map, with the lithologic units defined based on remote sensing characteristics in the visible, near-infrared, short-wave infrared, thermal infrared, and microwave regions. Figure 8 shows selected gray-scale image results of a Spectral Angle Mapper classification using the ROI defined as above. The brighter pixels represent better matches to the selected "spectra". Similar results could have been obtained with other classification techniques.

5.2 Field Reconnaissance

Field reconnaissance was conducted to examine some of the surfaces described above. Access to portions of this area is extremely difficult; the rougher alluvial fans are nearly impassable to foot travel. Areas A, B, C, D, and E were visited during April 1995 and the basic credibility of the geologic image map produced through analysis of the combined data set was confirmed. Fan B is a smooth carbonate alluvial fan with a well developed desert pavement surface. Fan A is the same composition as Fan B, however, it has been reworked and is extremely rough. Fan C is an elevated mixed quartzite composition fan with a well developed desert pavement and Fan D is the same composition as Fan C, but the pavement is gone, significant mixing occurs with other materials, and the surface is rough. Fan E is an active channel. The combined image dataset described here provides the best means for mapping this area because of its extended spectral coverage, its spatial coherency, and its ability to map even the roughest terrain.

Figure 8. Northern Death Valley 1995 Combined Optical Sar Data
Selected Spectral Angle Mapper Rule Image Results

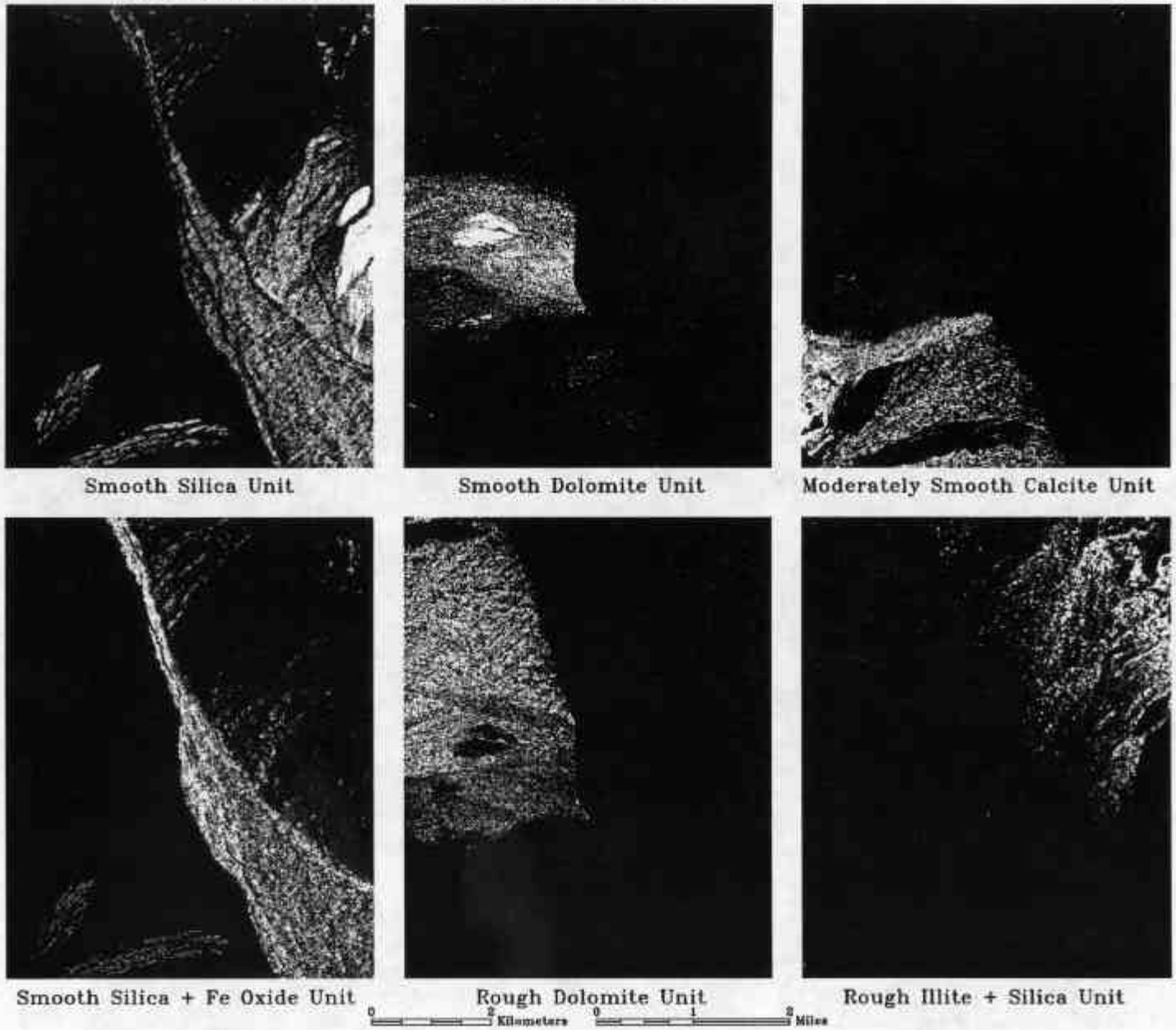

6. Conclusions

The units defined above provide a detailed picture of the surficial geology at the northern Death Valley study area. The surficial materials can be broken into several general compositions using the optical data; those with calcite, those with dolomite, and those with high silica contents, with or without iron oxides. The areas with dolomite include areas "A" and "B". Areas with significant amounts of silica, ranked in order of decreasing silica content, include areas "I", "J" and "C", "D", and "G". Typically, high iron oxide concentrations are associated with alluvial fans that appear smoother on the SAR data. This is probably the effect of desert varnish on older fans. There is a full range of surface roughness from very smooth to rough. The combined data sets allow discrimination of rough versus smooth carbonate and silica fans, a distinction not possible with only the optical data. The surface roughness, however, does not appear to be related to the presence or absence of either major rock forming mineral. The roughest surfaces correspond to active channels and where the various lithologies have been reworked by fluvial action.

This research has demonstrated the value of combined visible, near-infrared, short-wave infrared, thermal infrared, and SAR data for lithologic mapping. The combined data sets provide improved information return over any one of the individual sensors. This has significant implications for future remote sensing missions and sensors. It suggests that sensors such as ASTER could be used in combination with SAR systems for improved geologic mapping. This research also demonstrates that multispectral and hyperspectral techniques can be applied to combined optical/SAR data sets. Researchers analyzing similar data should consider available tools carefully to determine their applicability to their analysis problems. One of the most difficult problems facing scientists attempting to use these sensors for geologic mapping and other surface mapping problems is the availability and coregistration of data. Future systems should provide multispectral and/or hyperspectral coverage over a broad wavelength range and co-aregistered SAR. All these data sets should be inherently coregistered (preferably georeferenced) and provide regional coverage. When available, they will provide an efficient means of compiling both regional and detailed information for geologic mapping and map updates.

7. Acknowledgments

This research was sponsored by NASA/JPL Contract 960248. The author is a member of the SIR-C/X-SAR Science Team.

8. References

1. Boardman, J. W., 1993, Automated spectral unmixing of AVIRIS data using convex geometry concepts: in Summaries, Fourth JPL Airborne Geoscience Workshop, JPL Publication 93-26, v. 1, p. 11 - 14.
2. Boardman, J. W., and Kruse, F. A., 1994, Automated spectral analysis: a geological example using AVIRIS data, north Grapevine Mountains, Nevada: in Proceedings, ERIM Tenth Thematic Conference on Geologic Remote Sensing, Environmental Research Institute of Michigan, Ann Arbor, MI, p. I-407 - I-418.
3. Center for the Study of Earth from Space (CSES), 1992, Atmosphere REMoval Program (ATREM) User's Guide, Version 1.1, Center for the Study of Earth from Space, Boulder, Colorado, 24 p.
4. Kruse, F. A., Huntington, J. H., and Green, R. O, 1996, Results from the 1995 AVIRIS Geology Group Shoot: in Proceedings, 2nd International Airborne Remote Sensing Conference and Exhibition: Environmental Research Institute of Michigan (ERIM), Ann Arbor, v. I, p. I-211 - I-220
5. Green, A. A., Berman, M., Switzer, P, and Craig, M. D., 1988, A transformation for ordering multispectral data in terms of image quality with implications for noise removal: IEEE Transactions on Geoscience and Remote Sensing, v. 26, no. 1, p. 65-74.
6. Boardman, J. W., 1991, Sedimentary facies analysis; a geophysical inverse problem: unpublished Ph. D. Thesis, University of Colorado, 212 p.
7. Boardman, J. W., Kruse, F. A., and Green, R. O., 1995, Mapping target signatures via partial unmixing of AVIRIS data: in Summaries, Fifth JPL Airborne Earth Science Workshop, JPL Publication 95-1, v. 1, p. 23-26.
8. Boardman, J. W., 1996, Determination of image endmembers using an automatic pixel purity algorithm: in Proceedings International Symposium on Optical Science, Engineering, and Instrumentation (SPIE) 4-9 August 1996, v. 2819, (in press).
9. Evans, D. L. (ed.), 1995, Spaceborne synthetic aperture radar: Current status and future directions: A Report to the Committee on Earth Sciences Space Studies Board, National Research Council: NASA Technical Memorandum 4679, NASA Scientific and Technical Information Office.
10. Stoffan, E. R., Evans, D. L., Schmullius, C., Holt, B., Plaut, J. J., van Zyl, J., Wall, S. D., and Way, J., 1996, Overview of results of Spaceborne Imaging Radar-C, X-Band Synthetic Aperture Radar (SIR-C/X-SAR): IEEE Transactions on Geoscience and Remote Sensing, v. 33, no. 4, p. 817 - 828.
11. Sabins, F., F., 1987, Remote Sensing Principles and Interpretation: W. H. Freeman and Company, New York, 449 p.

12. Evans, D. L., Farr, T. G., Ford, J. P., Thompson, T. W, and Werner, C. L., 1986, Multipolarization radar images for geologic mapping and vegetation discrimination: IEEE Trans. Geoscience and Remote Sensing, v. GE-24, p. 246 - 257.
13. Elachi, C. 1987, Introduction to the Physics and Techniques of Remote Sensing: Wiley, New York, 413 p.
14. Jordan, R. L., Huneycutt, B. L:., and Werner, M., 1996, The SIR-C/X-SAR Synthetic Aperture Radar System:): IEEE Transactions on Geoscience and Remote Sensing, v. 33, no. 4, p. 829 - 839.
15. Palluconi, F. D., and Meeks, G. R., 1985, Thermal Infrared Multispectral Scanner (TIMS): An investigator's guide to TIMS data: Jet Pr opulsion Laboratory Publication 85-32.
16. Gillespie, A. R., Kahle, A. B., and Walker, R., 1986, Color enhancement of highly correlated images: I. Decorrelation and HSI-contrast stretches: Remote Sensing of Environment, v. 20., p. 209 - 235.
17. Kahle, A. B., and Goetz, A. F. H., 1983, Mineralogic information from a new airborne thermal infrared multispectral scanner: Science, v. 222, no. 4619, p. 24 - 27.
18. Rickman, D. L., and Grant, S. K., 1986, Nighttime TIMS, TMS, and chemical data from the Pyramid Mountains south of Lordsburg, New Mexico: in Proceedings of the Fourth Thematic Conference, International Symposium on Remote Sensing of Environment, Environmental Research Institute of Michigan, Ann Arbor, p. 363 - 364.
19. Kahle, A. B., 1987, Surface emittance, temperature, and thermal inertia derived from Thermal Infrared Multispectral Scanner (TIMS) data for Death Valley, California: Geophysics, v. 52, no. 7, p. 858 - 874.
20. Kruse, F. A., and Kierein-Young, K. S., 1990, Mapping physical properties of geologic materials by integration of diverse multispectral image data sets from the Geologic Remote Sensing Field Experiment (GRSFE), in Proceedings, IGARSS '90, College Park, Md, v. 2, p. 1351-1355.
21. Kruse, F. A., and Dietz, J. B., 1991, Integration of diverse remote sensing data sets for geologic mapping and resource exploration: SPIE Symposium on Remote Sensing for Geology and Geophysics, 1-5 April 1991, Orlando, Florida, v. 1492, p. 326-337.
22. Kierein-Young, K. S., 1995, Integration of quantitative geophysical information from optical and radar remotely sensed data to characterize mineralogy and morphology of surfaces: Unpublished Ph. D. Dissertation, University of Colorado, Boulder, 220 p.
23. Kierein Young, K. S., 1996, Integration of optical and radar data to characterize mineralogy and morphology of surfaces in Death Valley, California: IEEE Transactions on Geoscience and Remote Sensing (in press).